Understanding Hardness of Doped WB_{4.2}

Kirill D. Shumilov, Zerina Mehmedović, Hang Yin, Patricia Poths, Selbi Nuryyeva, leva Liepuoniute, Chelsea Jang, Isabelle Winardi, and Anastassia N. Alexandrova*

Department of Chemistry and Biochemistry, University of California, Los Angeles, Los Angeles, CA 90095-1569, USA

E-mail: ana@chem.ucla.edu

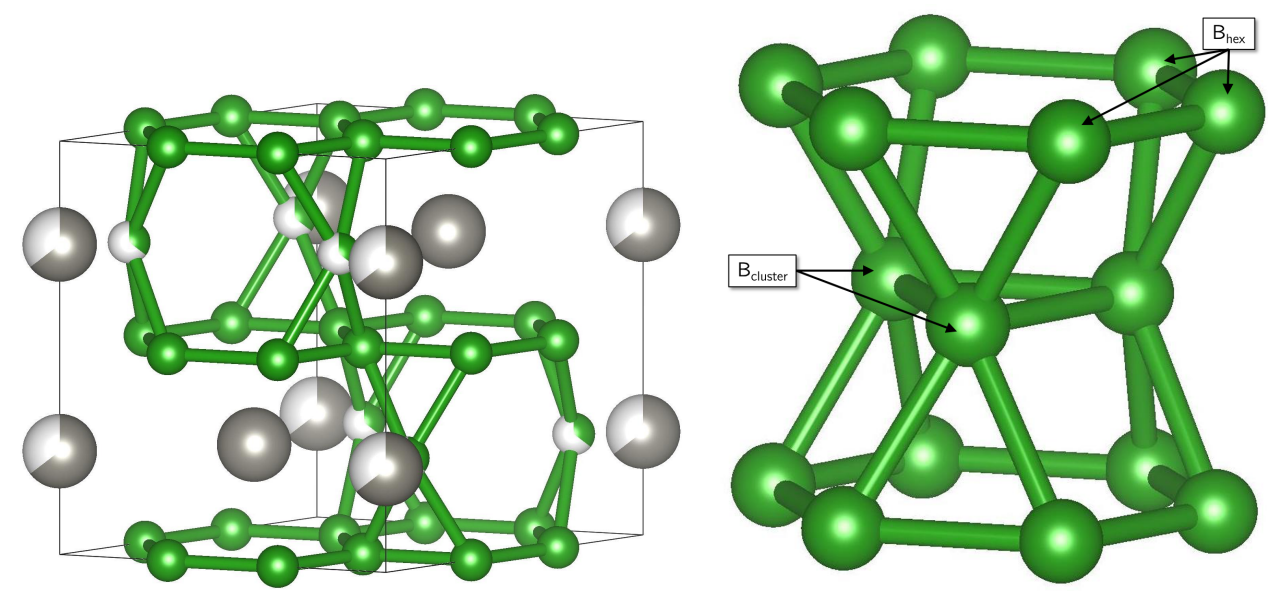
Abstract

WB_{4,2} is one of the hardest metals known. Though not harder than diamond and cubic boron nitride, it surpasses these established hard materials in being cheaper, easier to produce and process, and also more functional. Metal impurities have been shown to affect and in some cases further improve the intrinsic hardness of $\mathrm{WB}_{4.2}$, but the mechanism of hardening remained elusive. In this work we first theoretically elucidate the preferred placements of Ti, V, Cr, Mn, Zr, Nb, Mo, Hf, Ta in the WB_{4.2} structure, and show these metals to preferentially replace W in two competing positions with respect to the partially occupied B₃ cluster site. The impurities avoid the void position in the structure. Next, we analyze the chemical bonding within these identified doped structures, and propose two different mechanisms of strengthening the material, afforded by these impurities, and dependent on their nature. Smaller impurity atoms (Ti, V, Cr, Mn) with deeply lying valence atomic orbitals cause the inter-layer compression of WB_{4,2}, which strengthens the B_{hex}-B_{cluster} bonding slightly. Larger impurities (Zr, Nb, Mo, Hf, Ta) with higher-energy valence orbitals, while expanding the structure and negatively impacting the $B_{hex}-B_{cluster}$ bonding, also form strong $B_{cluster}-M$ bonds. The latter effect is an order of magnitude more substantial than the effect on the $B_{\rm hex}-B_{\rm cluster}$ bonding. We conclude that the effect of the impurities on the boride hardness does not simply reduce to structure interlocking due to the size difference between M and W, but instead, has a significant electronic origin.

Introduction

Transition metal borides posses many of extremely useful mechanical properties such as high hardness, incomprehensibility, and temperature and wear resistance. ^{1–4} A number of transition metal borides have Vicker's hardness greater than 40 GPa and bulk modulus larger than 300 GPa, which, coupled with their metallic nature and inexpensiveness, makes them excellent materials for superhard coating and cutting tools. ^{5–8}

A vast number of superhard metal borides with various crystal structures has been discovered in recent years, including mono-, ^{8,9} di-, ^{5,6,10} tetra-, ¹¹⁻¹⁴ and dodecaborides, ^{15,16} as well as their solid solutions. It has been experimentally shown that the hardness of materials of this class can be controlled through *intrinsic*—originating from local chemical bonding—and *extrinsic*—resulting from surface grain boundaries and pattering—hardening effects. In this light, tungsten tetraboride stands out for its cost-effective synthesis and tunable hardness through addition of dopants. ¹⁵



(A) $WB_{4.2}$ unit cell. Partially colored atoms indicate partial occupancy.

(B) Hourglass structure, formed by bonding between two hexagonal boron layers (B_{hex}) and B_3 cluster.

Figure 1: Structure of WB_{4.2} with $P6_3/mmc$ space group, ICSD 291124. Boron atoms are colored in green, tungsten atoms are colored in gray; partially shaded atoms are partial occupancy sites that can be occupied by tungsten or B₃.

A number of transition metal impurities have been shown to enhance tungsten tetraboride's hardness and incomprehensibility intrinsically (Ti, Hf, Ta, Mo, etc.) and extrinsically (Zr, Y, Sc, Mn, etc.) 11,13,14,17,18 Despite ample experimental data, theoretical predictions of novel superhard tungsten tetraboride solid solutions has proven to be complicated. WB_{4.2} posses a unique disordered crystal structure (Fig. 1A). It consists of alternating layers of hexagonal boron sheets (B_{hex}) and W atoms, with some of W substituted by B₃ clusters (2 clusters

per 3 unit cells). ^{19,20} The presence of B₃-trimers is crucial in the formation of the interlayer 3D-covalent boron-boron bonding network (so-called "hourglass" structures, Fig. 1B), which has been hypothesized to be responsible for the exceptional mechanical properties of the material, and particularly preventing the slip along the most "slippery" slip system. ^{21,22} However, the disorder embedded in the system presents a considerable challenge to pinpoint the bonding effects behind materials hardness, especially in the case of doped WB_{4.2}. Little is known about the preferred locations of various transition metal dopants in the tungsten tetraboride lattice, as well as their influence on the key hypothesized hardening element in this lattice—the hourglass structure. Understanding these structural and electronic effects of adding different transition metal impurities to the tetraboride is essential in the rational design of novel superhard materials.

In this work, we investigate effects of transition metal impurities (Ti, Zr, Hf, V, Nb, Ta, Cr, Mo, and Mn) on the chemical bonding within a WB_{4.2} model structure, containing a single B₃-trimer. Through the use of *ab initio* Density Functional Theory (DFT), coupled with Quantum Theory of Atoms and Molecules (QTAIM) and Crystal Orbital Hamiltonian Population (COHP) analysis, we study the preferred position of the impurity, as well as its qualitative and quantitative effect on the inter-layer bonding, in relation to material's hardness.

Computational Methods

All calculations have been performed using the DFT Perdew-Burke-Ernzerhof (PBE) 23,24 Generalized Gradient Approximation (GGA) functional with the D3 25 dispersion correction, as implemented in Vienna *Ab-initio* Software Package (VASP) $^{26-29}$ (See Supporting Information, Choice of DFT functional). A 520 eV energy cutoff was used with $3 \times 3 \times 6$ Γ -centered Monkhorst-Pack k-points grid. Spin-polarized two-step geometry optimization was performed with $2^{\rm nd}$ order Methfessel-Paxton smearing ($\sigma = 0.15$) for each structure until

all atomic forces were $\leq 0.005\,\mathrm{eV/Å^2}$. Each geometry optimization was followed by a static energy calculation using tetrahedron method with Blöchl corrections until the change in atomic energy was $\leq 1.0\times 10^{-8}\,\mathrm{eV}$. We additionally performed the c-normal strain distortion calculations, by consecutive application of a $\varepsilon=0.1$ engineered strain, starting from the ground state structure.³⁰

QTAIM calculations were performed using the Critic2^{31,32} software. Electron density for QTAIM calculations was obtained from special static VASP calculations with double the number of grid points in the FFT-grid. Identification of critical points was based on recursive subdivision of the Wigner-Seitz cell algorithm. Atomic basin interactions to calculate atomic Bader charges utilized Yu and Trinkle (YT)³³ method.

ICOHP calculations have been performed using the Lobster^{34–37} package. Wavefunctions for ICOHP were taken from special static VASP calculations with twice as many bands as normal calculations. pbeVaspFit2015³⁶ basis set was used to achieve $\leq 1.8\%$ average absolute charge spilling.

Results & Discussion

Impurity Placement

A simple WB_{4,2} $2 \times 2 \times 1$ supercell with a single B₃-trimer (221.1B3) substituting one of W (Fig. 2A) has been chosen to carry out the majority of calculations. Despite the non-experimental ratio of B to W (one B₃-trimer per four unit cells, instead of four B₃-trimers per six unit cells) this model was more affordable, and allowed us to explore more extensively the position of the impurity, while did not prevent understanding the local bonding effects of (M) within the material.

We began our search by investigating the various positions that M can occupy. Based on our model structure, the impurity can occupy one of only five unique positions, substituting W at various distances with respect to the B₃ cluster, listed in Table 1 and shown in Fig. 2.

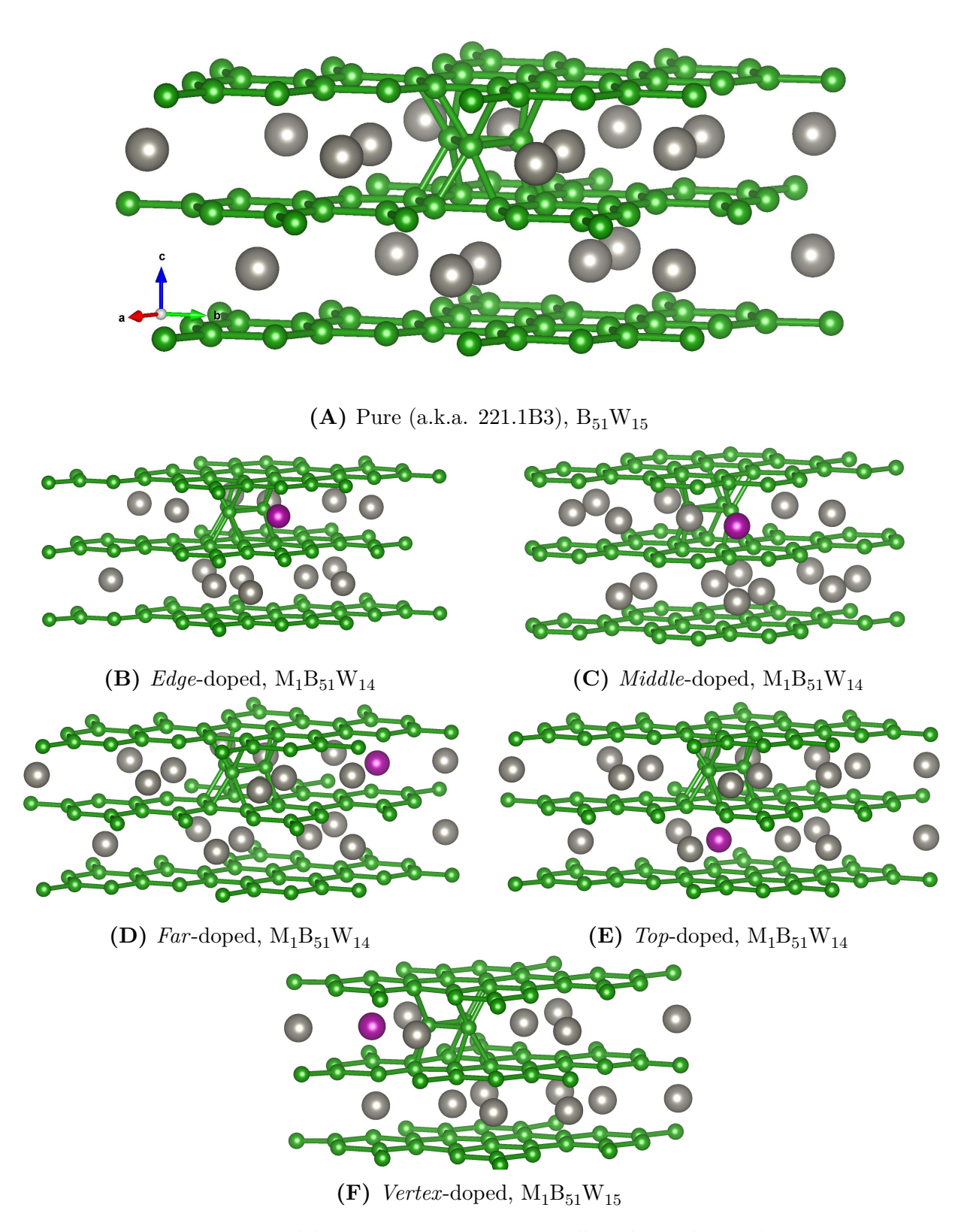


Figure 2: Model $WB_{4.2}$ 2 × 2 × 1 supercell with single B_3 cluster.

Table 1: Distances between center of B_3 -cluster and the metal impurity substituting W-atom in different positions in $WB_{4,2}$ $2 \times 2 \times 1$ supercell with single B_3 .

Position	Distance, Å	Layer	Impurity Type
Vertex	2.96	Same as B_3 -cluster	Interstitial (inserts into W void)
Edge	2.96		Substitutes W
Middle	5.17		
Far	5.97		
Top	3.15	Different layer	

Structures with impurities at different positions were geometrically optimized and their energies of formation from the pure bulk boron and bulk metals were calculated for each structure (Fig. 3). Despite the lack of the zero-point energy corrections to the energies, the calculated energies of formation combined with the volume information clearly indicated the presence of strong bonding changes, occurring with the addition of the impurity. The volume change (Fig. 3B) shows strong dependence on the atomic radius of the impurity, regardless of the position of the impurity. Indeed, it can be noticed that generally fourth row elements, possessing smaller atomic radii, cause contraction of the structure, while larger elements, such as Zr and Hf, cause the cell to expand. The change in volume occurs mostly through elongation or shortening along the c-axis, or, in other words, through distance change between the hexagonal boron sheets, relative to the initial model structure (Fig. 2A). Notice that vertex-doped structures (i.e. structures where the impurity occupies the void in the lattice) are generally associated with larger volumes and energies of formation, relative to the initial model structure. This observation suggests that placing the dopant in the void of the parent boride is considerably unfavorable. For this reason, we do not focus on the vertex-doped structures in the rest of the paper, though include the computed properties for these structures, for completeness. For all other positions, we see that almost all dopants (except Cr and Mn) have smaller ΔE_f than that of 221.1B3. The lack of clear correlation between the energy of formation and atomic size of the impurity points to the presence of additional chemical bonding effects in the cases of substitutional doping. Interestingly, the alteration in the position of the impurity for substitutional doping does not change the volume, or the energy of formation significantly (overall variation between positions for a single dopant is $\leq 2.0\,\mathrm{eV}$).

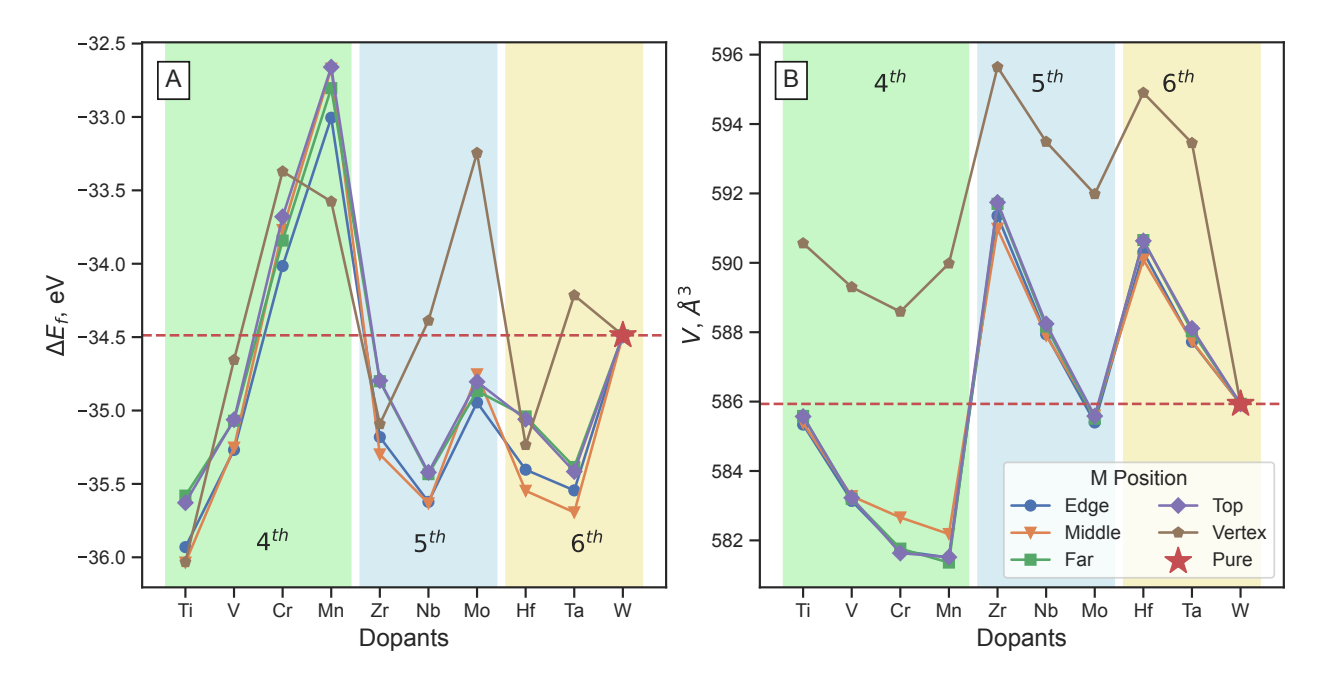


Figure 3: Formation energy (A) and volume (B) of doped model structures. The shade of the background indicates the period of the dopant.

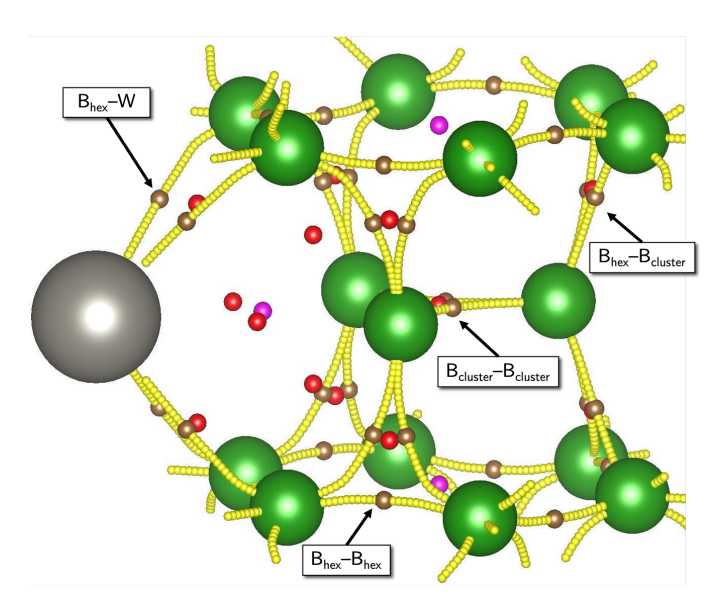
Due to the lack of differentiation based on ΔE_f between the substitutional impurities in different positions, we now focus on the specifics of the electronic structure in both the edge and the middle configurations. These positions are additionally chosen such that the interaction between the cluster and the impurity is substantial, since the clusters have been hypothesized to contribute to the boride hardness. The edge position is especially interesting due to its proximity to the B_3 cluster, suggesting the biggest impact on its bonding.

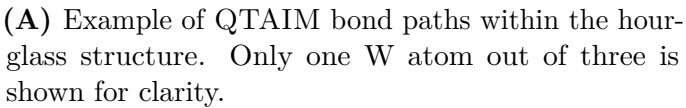
Chemical Bonding

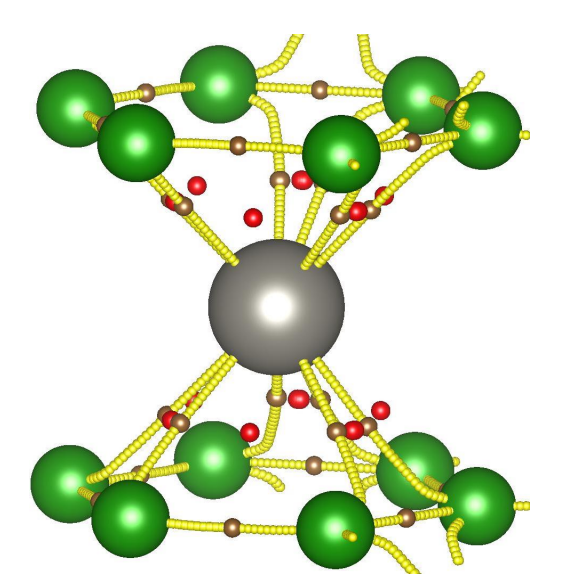
QTAIM

To explore the underlying chemical bonding effects, and particularly the nature of the interactions between M, W, B₃, and hexagonal boron layers, we first employ QTAIM, the

Quantum Theory of Atoms and Molecules, a mathematically rigorous formalism to analyze the properties of the electron density, and connect those to chemical properties. The eigenvalues of the Hessians of critical points (CPs) in the charge density—points where all three first derivative of the density with respect to spatial coordinates vanish—reveal the bonding information. There are 4 types of crictial points in three-dimensional space: nuclear critical point (NCP) with all three Hessian eigenvalues positive, bond critical point (BCP)—two eigenvalues positive, ring critical point (RCP)—two eigenvalues negative, cage critical point (CCP) with all three Hessian eigenvalues negative. In this work, we primarily focus on BCPs and their properties. Each BCP is connected via bond paths to two NCPs, associated with two different nuclei in the cell. Two properties are commonly used to qualitatively compare BCPs: the electron density (ρ) and the Laplacian of the electron density ($\nabla^2 \rho$). A stronger bond would generally have a high electron density and a more negative Laplacian at its BCP, while a weaker bond would generally have a smaller electron density and a more positive Laplacian.







(B) Example of QTAIM bond paths around the W atom.

Figure 4: QTAIM plots for the pure model structure. BCP points are colored in brown, RCP—in red, CCP—in magenta. Bond paths are shown in sequences of yellow points.

Relevant QTAIM graphs for model structures are shown in Fig. 4. The QTAIM graphs of model structures with impurities did not differ significantly in the geometry of critical points and, thus, are not shown. The properties of BCPs ($B_{hex}-B_{cluster}$, $B_{hex}-W$, $B_{hex}-M$), connecting boron hexagonal layers, are shown in the Fig. 5 (See Supporting Information Figure S1 for additional information.) Bader charges calculated for the B_3 -trimers and W atoms are shown in Fig. 6.

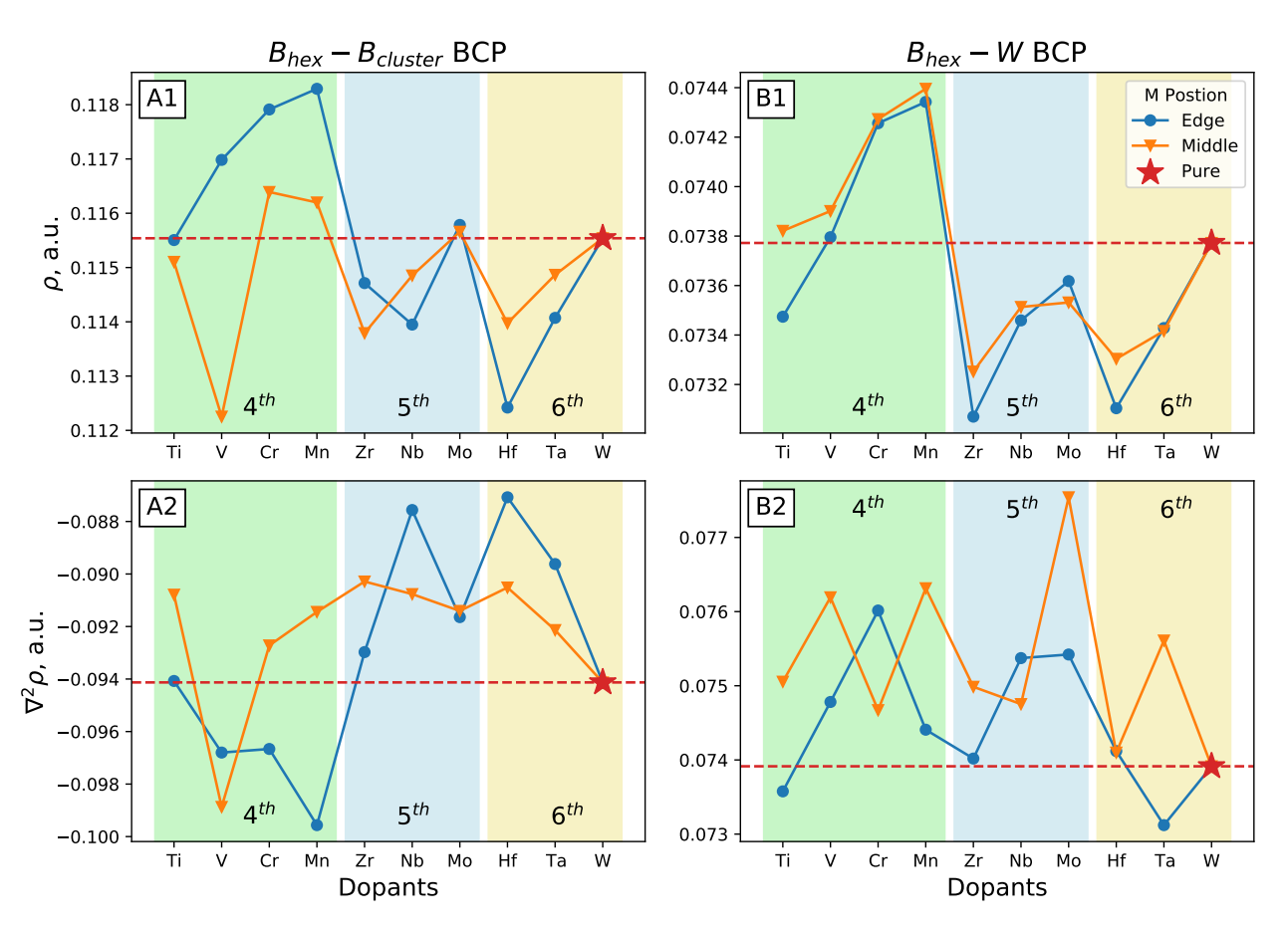


Figure 5: QTAIM analysis of *edge*-doped and *middle*-doped model structures. (A1) Average electron density and (A2) Laplacian at $B_{\text{hex}}-B_{\text{cluster}}$ BCP. (B1) Average electron density and (B2) Laplacian at $B_{\text{hex}}-W$ BCP.

From Fig. 5 A1,B1, as well as Fig. 6, one can see the similar "climbing zig-zag" trend as the one observed in the changes of the volume (Fig. 3.) The trend is better visible in the cases of edge-doped structures, especially in such BCP properties as ρ and the Bader charge. The trend is less noticeable for $\nabla^2 \rho$. The "climbing zip-zag" pattern could be linked to the atomic

radius of the impurity and its proximity to the cluster. We see that the smaller impurities are generally associated with larger ρ at the inter-layer BCPs and more negative $\nabla^2 \rho$, as well as more positively charged B₃ and more negatively charged impurity. The shorter distances of the impurity to the cluster strengthen the effects of the smaller atomic radii, and larger distances weaken them.

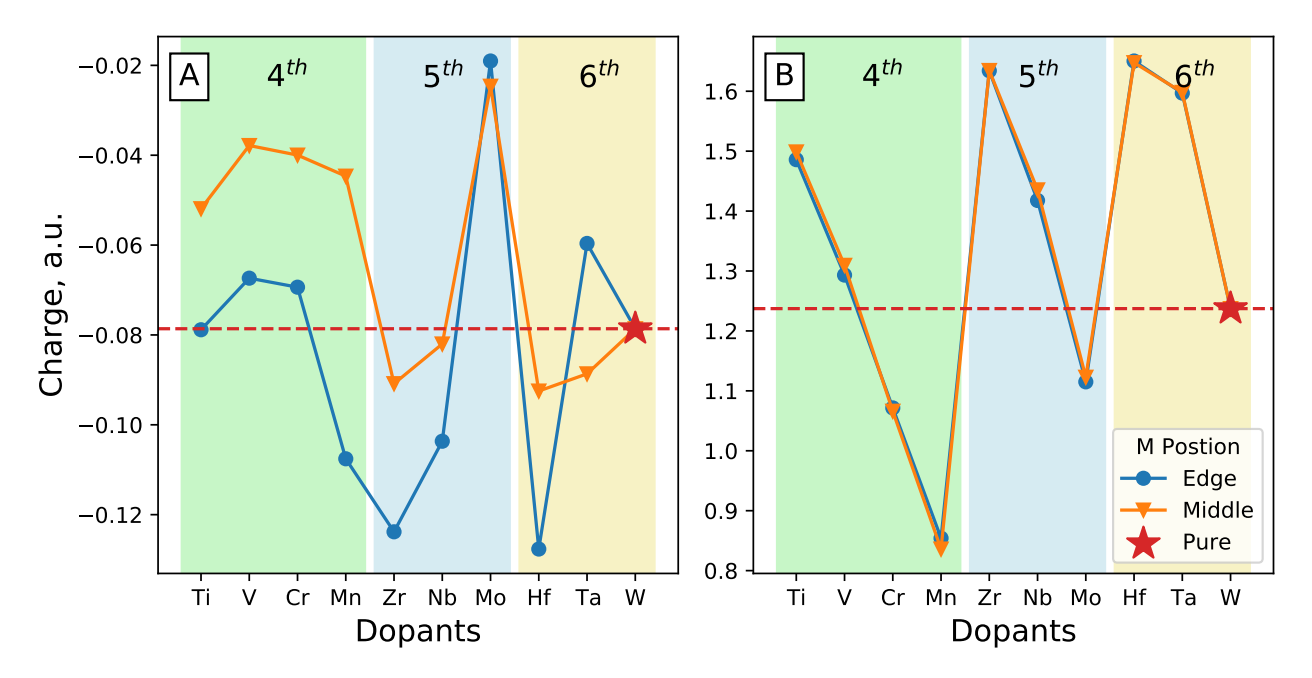


Figure 6: QTAIM analysis of *edge*-doped and *middle*-doped model structures. (A) Total Bader charge on the B₃-cluster. (B) Average Bader charge on W atoms.

However, for the purposes of this study, QTAIM analysis is insufficient, because it does not directly provide energetic information, and therefore, allows for only qualitative comparisons between different types of bonds, or relative to some "standard." Furthermore, CP evaluation in QTAIM relies on the integration and differentiation of electron density, implemented on a grid for periodic systems, and therefore bearing some inaccuracy, especially when CP are proximal. WB_{4.2} is prone to such errors. As we can see from small negative $\nabla^2 \rho$ (Fig. 5), a great number of bonds in the system are electron-deficient, resulting in very curved bond paths (Fig. 4). The CPs defining these paths appear to "merge" into a single CP for some systems, due to their proximity and the insufficient resolution of the electron density grid. Thus, we use QTAIM only to guide our search for the bonding mechanism in

WB_{4.2}, but not for the evaluation of the relative strengths of the key bonding effects.

COHP and ICOHP

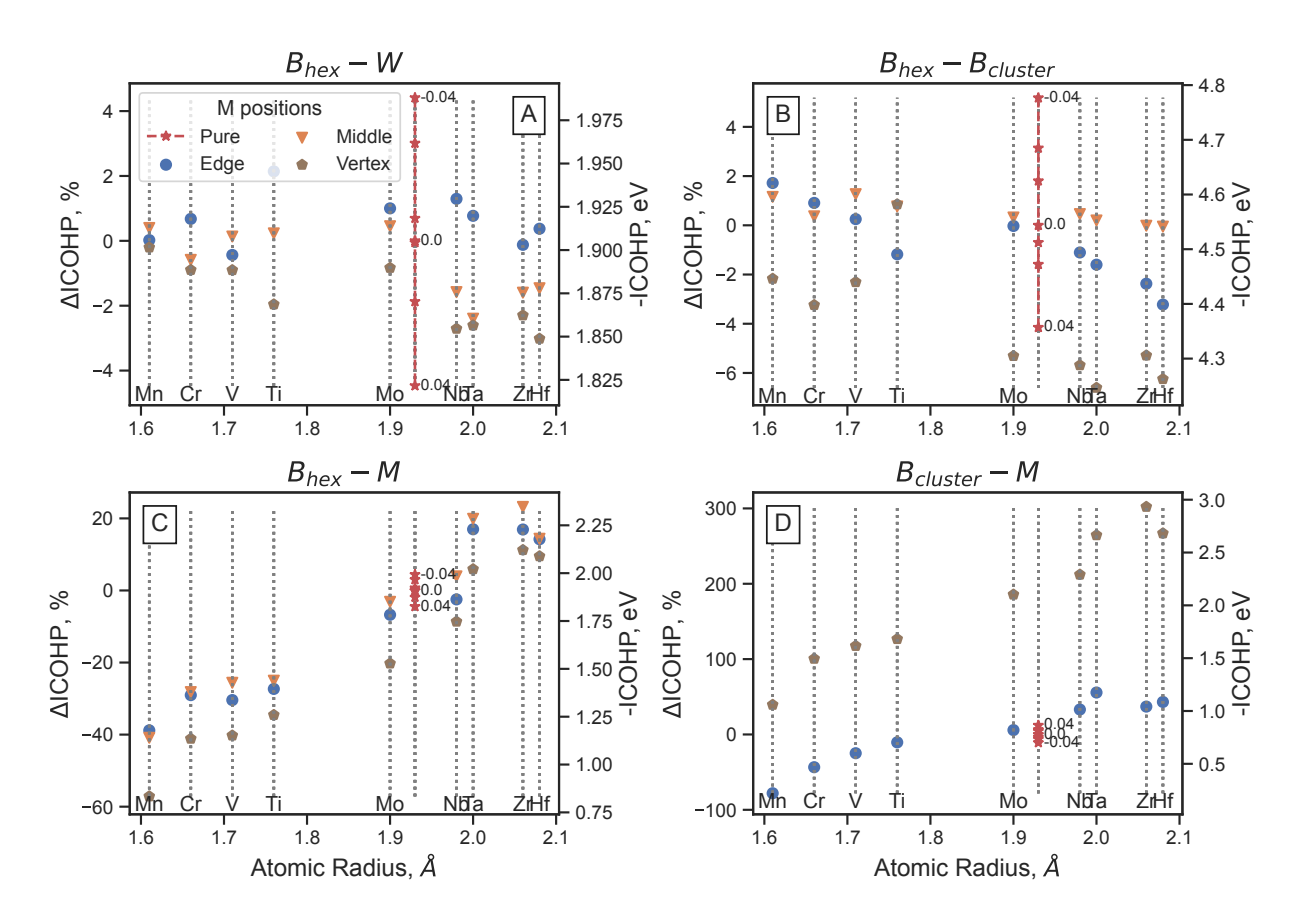


Figure 7: Comparison of the pure c-strained model structure (red, with the stress values labeled), the edge-doped (blue), middle-doped (orange), and vertex-doped model structures. Average bond ICOHP of (A) B_{hex} —W bond, (B) $B_{cluster}$ —W bond, (C) B_{hex} — B_{M} bond, and (D) $B_{cluster}$ —M bond as a function of the atomic calculated radius ³⁸ of the impurity metal. The numbers next the pure line indicate the engineered strain, applied along the c-axis of pure model structure. Left y-scale indicates Δ ICOHP as defined by Eq. 1 and right y-scale indicates absolute value of —ICOHP.

COHP analysis was done to assign energetics to the bonds found by QTAIM. COHP analysis works by partitioning the band structure of a crystal into pair-wise energy-weighted orbital interactions. By integrating COHP up to the Fermi level, one can obtain a good estimation of a bond strength in a solid-state. More negative ICOHP values are associated with stronger bonds, and vice-versa. By averaging ICOHP over bonds identified by QTAIM,

we can estimate the changes in stability upon addition of an impurity.

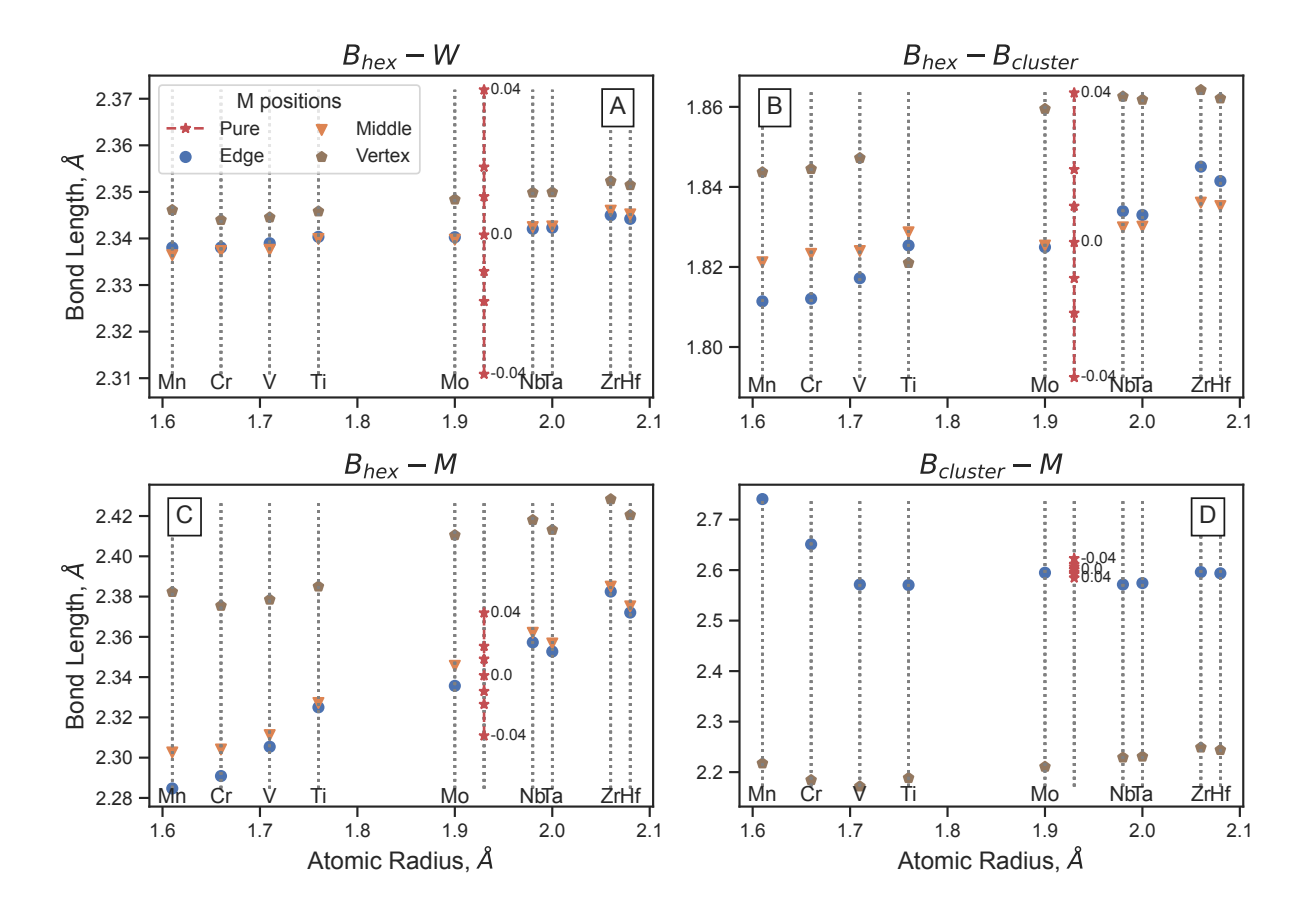


Figure 8: Comparison of the pure c-strained model structure, edge-doped, middle-doped, and vertex-doped model structures. The average bond length of (A) B_{hex} –W bond, (B) $B_{cluster}$ –W bond, (C) B_{hex} – B_{M} bond, and (D) $B_{cluster}$ –M bond, as a function of the calculated atomic radius³⁸ of the impurity. The numbers next the pure line indicate the engineered strain, applied along the c-axis of pure model structure.

Here, we aim to deconvolute the effect of the size of the impurity atom from the additional bonding effects that the impurity brings. Therefore, as a purely theoretical reference, we applied a set of normal strains ($\epsilon \in [-0.04, -0.02, -0.01, 0.01, 0.02, 0.04]$) along the c-axis of the pure model structure, to mimic the incorporation of the impurities of all sizes, from small to large, but without additional electronic effects. We relaxed all degrees of freedom in the strained structures, and calculated ICOHP (vertical red lines in Fig. 7 and Fig. 8). For edge-, middle-, and vertex-doped structures the analogous analysis was performed (Fig. 7 and

Fig. 8). The y-axis in Fig. 7, is calculated according to the formula:

$$\Delta ICOHP_i = \frac{ICOHP_i - ICOHP_{pure}}{ICOHP_{pure}}$$
 (1)

Vertex-doped structures was included in the COHP and ICOHP calculation to further prove that interstitial doping is unfavorable and leads to destabilization. In the Fig. 7, we, indeed, see that generally vertex-positioned impurities cause decrease in the strength of all inter-layer bonds, as compared to pure and edge-, middle-doped structures.

For the case of substitutional doping, we can see that on average the strongest inter-layer bond is $B_{\text{hex}}-B_{\text{cluster}}$, followed by $B_{\text{hex}}-W$ and $B_{\text{hex}}-M$ of competitive strengths. Firstly, the addition of an impurity in any position has little effect on the strength and length of the $B_{\text{hex}}-W$ bonds (Fig. 8A), suggesting that the equilibrium inter-layer separation in the boride is defined by that bond length. On the other hand, the strongest bond, $B_{\text{hex}}-B_{\text{cluster}}$, is sensitive to the nature and position of the impurity. While it experiences a rather little change in ICOHP in the case of the *middle* doping, a significant change is seen in the case of the *edge* doping. Moreover, the impurities can be classified as two types: the 4th period elements (Ti, V, Cr, Mn), and the later period elements. Both types quite linearly affect the $B_{\text{hex}}-B_{\text{cluster}}$ distance and bond strength as functions of the atomic radius of the impurity, though to a slightly different degree. As the impurity atoms gets larger, the cluster-layer boron bonding weakens. Therefore, the boron-boron bonding in the parent tetraboride appears to be slightly compromised by the large size of the W atom, which adds a strain to the structure by separating the boron layers and clusters more than their equilibrium distance would be without W in the lattice.

The biggest difference is seen in the $B_{\text{hex}}-M$ bonds. Contrary to the $B_{\text{hex}}-B_{\text{cluster}}$ bond, the $B_{\text{hex}}-M$ bond is stronger for the latter period impurities in the *edge* and *middle* positions. Note that the bond strength change is more dramatic than for the $B_{\text{hex}}-B_{\text{cluster}}$ bonds, and constitutes the most significant electronic structure impact of the impurity on the boride. To

summarize, we see that the 4^{th} period elements strengthen the $B_{hex}-B_{cluster}$ bonds by bringing the clusters and layers of boron closer together and apparently enhancing the covalent bonding overlap (presumably therefore strained by the larger W atoms in the undoped boride). On the contrary, the 5^{th} and 6^{th} period elements increase the boron cluster-layer separation and adversely affect the bonding there, but are capable of strong $B_{hex}-M$ bonding interactions that counterbalance the effect (Fig. 8.) In addition, we observe the $B_{cluster}-M$ bond in some cases, which is overall very weak, though marginally stronger for the latter period elements, as will be shown shortly.

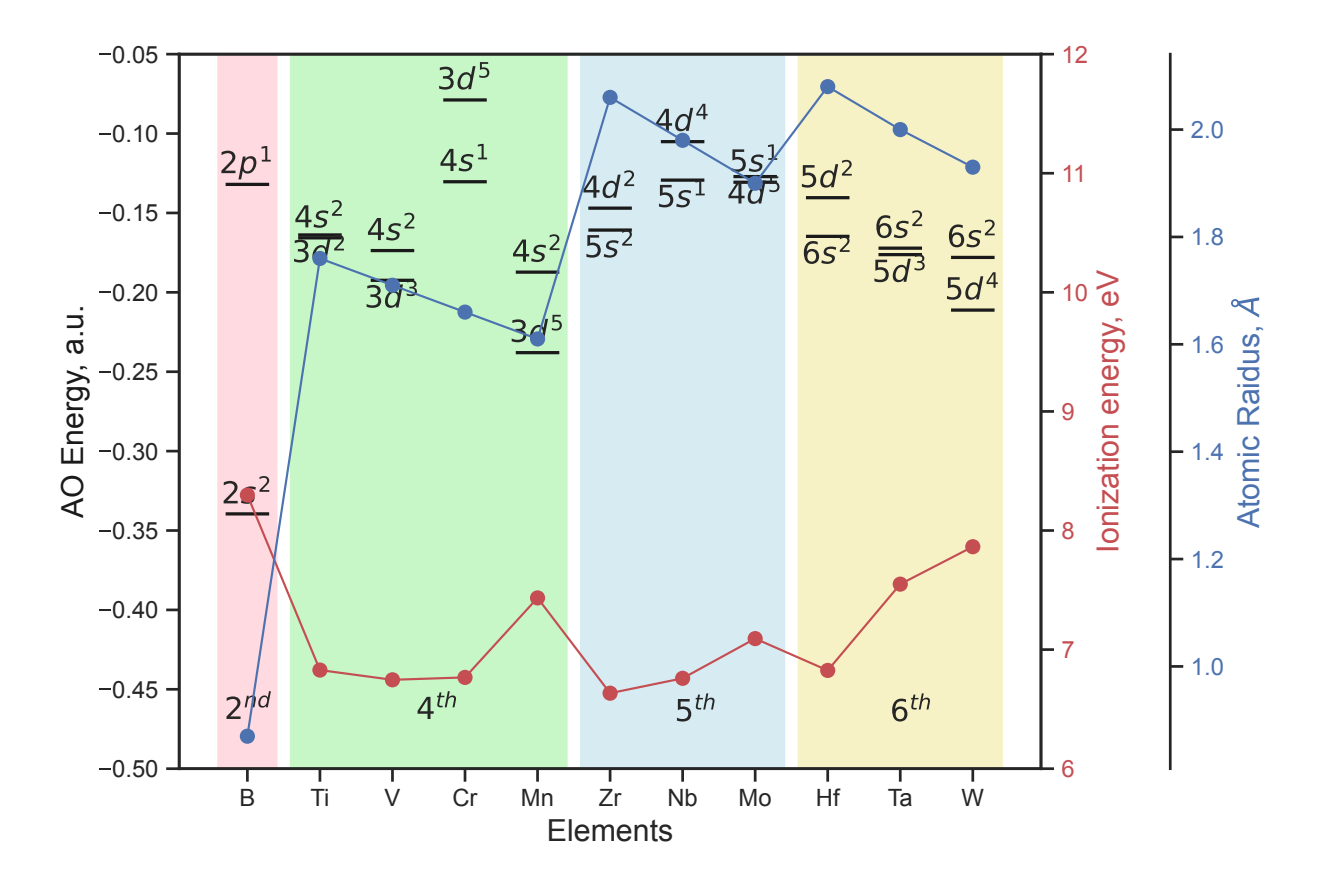


Figure 9: Energies of valence AO orbitals, ^{39–41} 1st ionization energy, ⁴² and calculated atomic radii ³⁸ of the elements of interest.

A possible explanation of the appearance of the bonds between some impurities and the hexagonal boron layer may be found in the comparison of valence atomic orbitals (Fig. 9.) The 4^{th} period elements have generally lower lying valence orbitals, especially, 3d, which can

be significantly lower than B's 2p (except for Cr). They are also small atoms, presumably differing in the bonding overlap with the boron. As a result, the elements in the 4^{th} period form poor bonds with both B_{hex} and $B_{cluster}$ atoms. They act primarily as a means to reduce the interlayer bond distance and allow B_3 clusters bind better with B_{hex} layer. This explains the reduction in the B_3 Bader charge and stronger $B_{hex}-B_{cluster}$ bonds. The 5^{th} and 6^{th} period elements, on the other hand, bind better to both the clusters and the hexagonal boron layers, with hexagonal layer bonding being more preferable, regardless of the position of the impurity. The simultaneous weakening of $B_{hex}-B_{cluster}$ can be a product of increased separation and the slight π -back donation onto metal's d orbitals.

Therefore, we propose two intrinsic hardening mechanisms for the tetraboride, based on different types of impurities. The 4^{th} period elements enhance the $B_{hex}-B_{cluster}$ bonding by bringing B_{hex} layers closer together, and in this way stiffening the main slip system in the material. This effect is most noticeable in when M occupies the *edge* position—closest to the B_3 cluster. However, it does little in the *middle* position, where the local distortion is far from B_3 . We can hypothesize that the effect might eventually lead to favoring the *edge* placement of the impurity with respect to the clusters during synthesis, and/or affect the concentrations of the boron clusters in the doped structure (i.e. the level of the stoichiometric excess of boron). The 5^{th} and 6^{th} period elements bind well to the boron hexagonal layers, forming stronger bonds with the layers than does W itself. This effect can be substantiated by the COHP analysis (Fig. 10.)

To further illustrate the mechanism, we calculated the COHP and ICOHP, for the binding to the boron layer for the two impurities that represent the two proposed intrinsic hardening mechanisms (Mn and Hf) (Fig. 10). We compare the COHP and ICOHP of the B_{hex} -M bond for the pure model structure, and Hf and Mn *middle*-doped structures. The reason we picked this doping position here is to see the effect in isolation from the possible interactions of the impurity with the boron cluster. We can see that low lying Mn s and d orbitals, its smaller size, and its greater number of d-electrons do not favor the the bonding

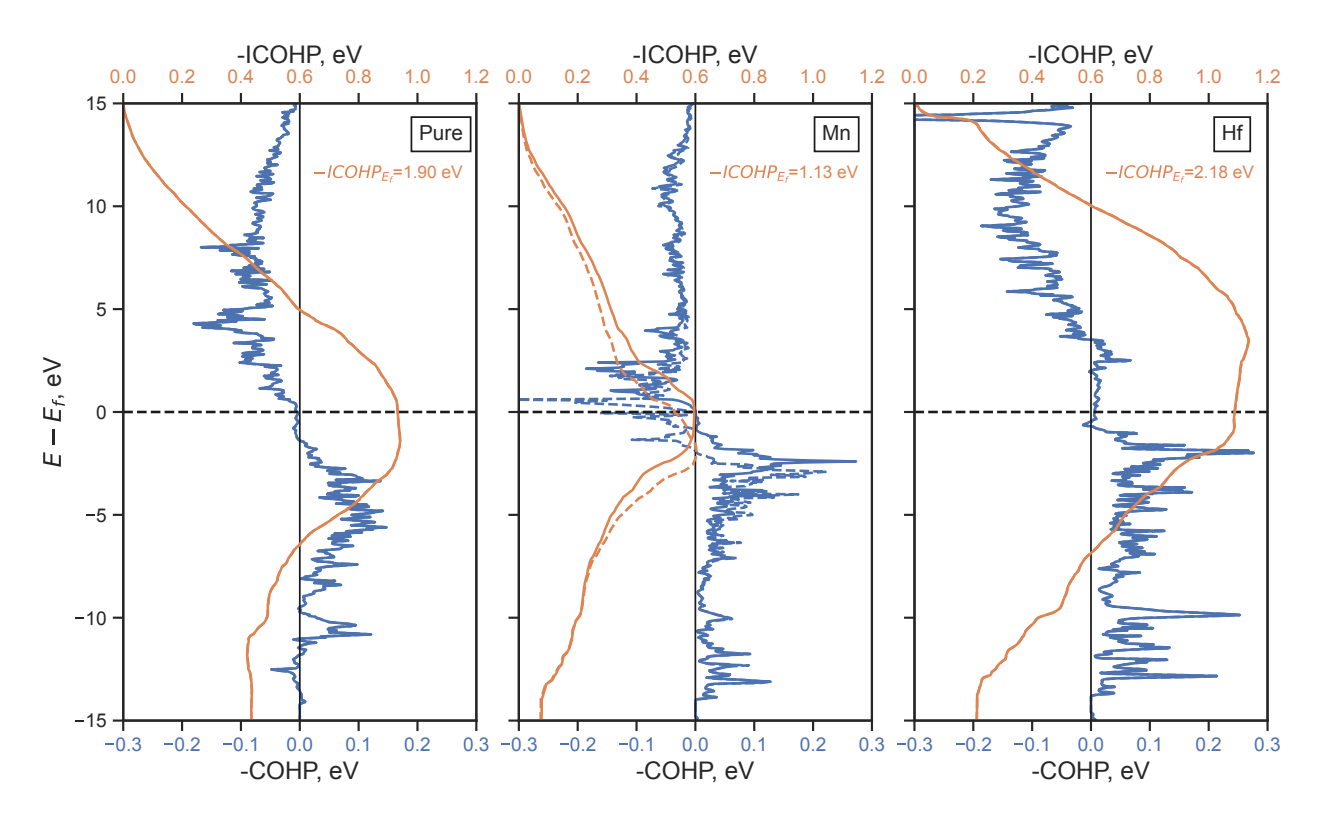


Figure 10: COHP and ICOHP of B_{hex}-M (B_{hex}-W for pure structure): ("Pure")—pure structure, ("Mn")—middle-doped with Mn, ("Hf")—middle-doped with Hf. For all graphs, blue curve corresponds to -COHP, with axis on the bottom, and orange—to ICOHP with axis on the top.

with the boron layer, featuring the population of the anti-bonding states (seen below the Fermi energy). The B_{hex} -Mn bond is thus the weakest of the three considered in the Figure. On the other hand, Hf (higher d-AO, fewer d-electrons, and lager size) forms a significantly stronger bond with the boron layer, with a major bonding character seen below the Fermi level, and all of the anti-bonding states appearing above the Fermi level. Since some bonding states appear above the Fermi level in this case, the material could be made stronger if a chemical mechanism could be found to donate slightly more electrons into this bond.

The COHP and ICOHP for the $B_{hex}-B_{cluster}$ bond are compared in Fig. 11 for the pure model, and the Hf and Mn *edge*-doped structures. In this case, the placement of the impurity is chosen such that the effect on the cluster-layer bonding is most pronounced. All three graphs look very similar, indicating that the impurities do not dramatically affect the nature of the $B_{hex}-B_{cluster}$ bonding, i.e. do not pump or remove electrons from this bonding region.

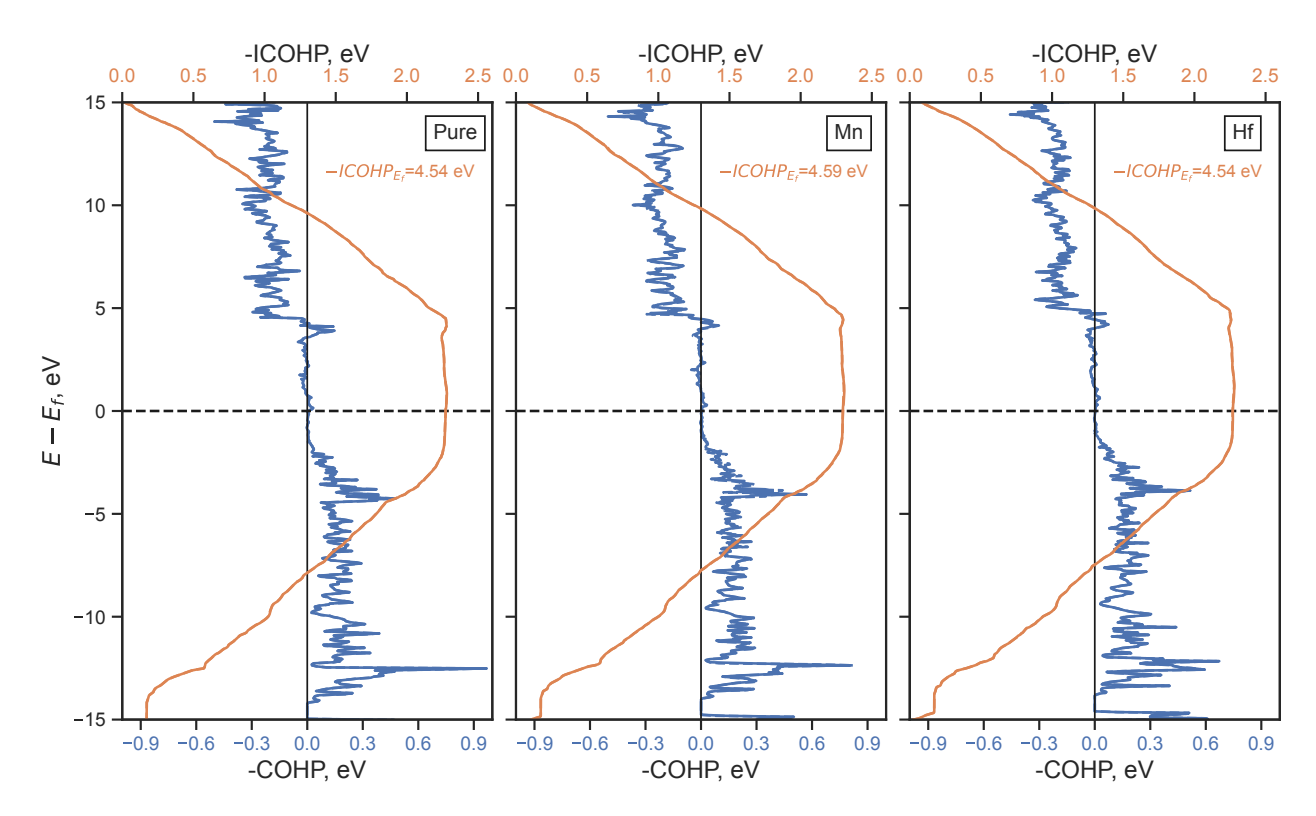


Figure 11: COHP and ICOHP of B_{hex}-B_{cluster} bond orbitals: ("Pure")—pure structure, ("Mn")—edge-doped with Mn, ("Hf")—edge-doped with Hf. For all graphs, blue curve corresponds to -COHP (axis at the bottom), and orange—to ICOHP (axis at the top).

Instead, yet again, the effect of the impurities boils down to affecting the quality of the covalent overlap via changing the bond length, or inter-layer distance, through the size of the impurity. Finally, Fig. 12, depicts COHP and ICOHP for the B_{cluster}-M bond comparing the pure model, and the Hf and Mn *edge*-doped structures. The placement of impurity in this Figure is the same as in Fig. 11. This bond is very weak for all structures, and does not constitute a major effect in the materials.

We note that, in metallurgy literature, the hardening effect of impurities is most typically attributed to structure locking upon slip to the impurity atom size mismatch. However, here, it is evident that the impurity also affects the bonding within the material. While the impurities affect the boron-boron inter-layer bonding to a small degree, the ability of the impurity itself to bind to the boron layers is a more dramatic effect, and we anticipate it to be important for the mechanical properties of the doped materials. From that point of

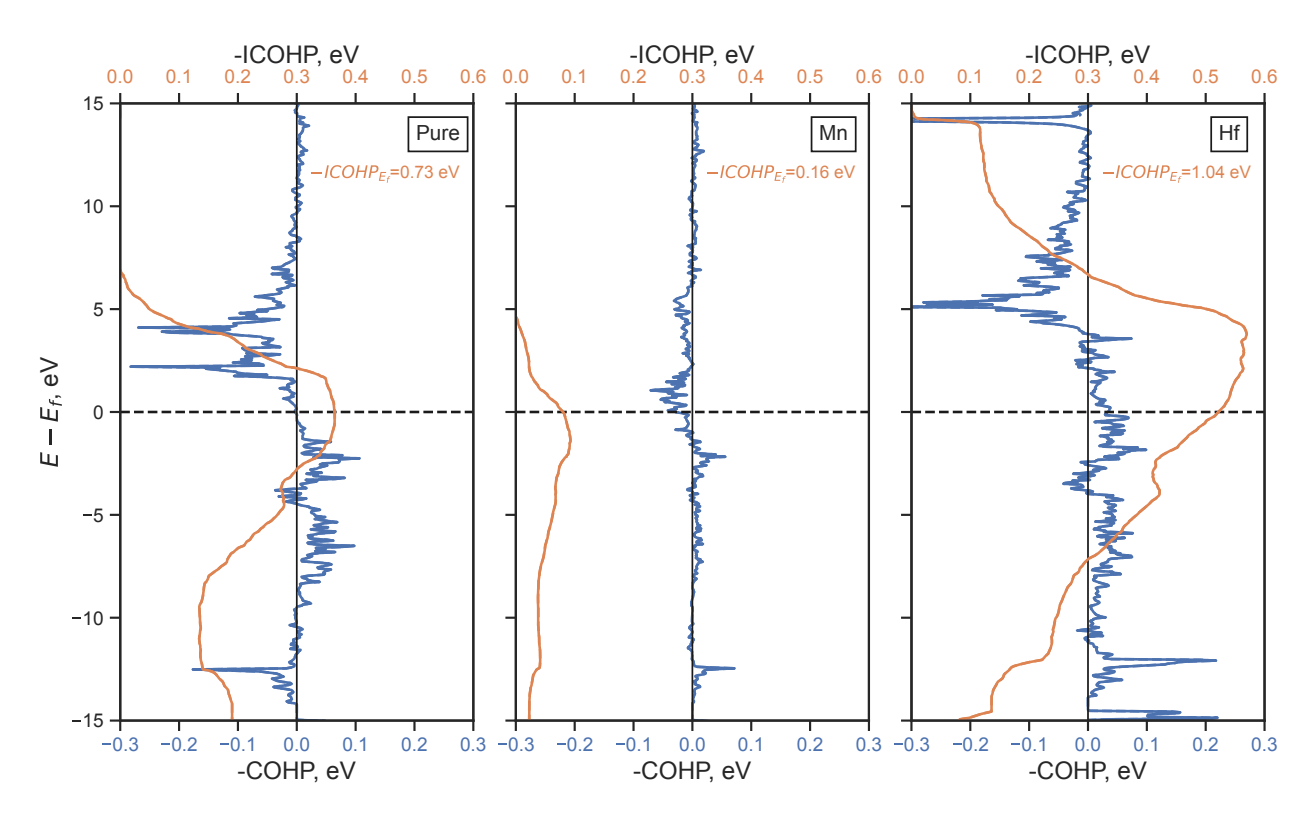


Figure 12: COHP and ICOHP of B_{cluster}-M (B_{cluster}-W for pure structure): ("Pure")—pure structure, ("Mn")—edge-doped with Mn, ("Hf")—edge-doped with Hf. For all graphs, the blue curves correspond to -COHP (axis at the bottom), and the orange—to ICOHP (axis at the top). Dotted and solid lines are associated with different spins.

view, an "ideal" dopant would be smaller than W to enhance the cluster-layer boron-boron bonding, yet itself binding to the boron more strongly than W. If the two bonding effects (metal-layer and cluster-layer bonding) work against each other for a particular impurity, their compounded effect on material's hardness will depend on the stoichiometry (to be studied in the future). Our results might also imply that the anisotropic compression of the parent tetraboride along the c axis might strengthen the material against slip, as the boron-boron bonding would be made stronger.

Conclusion

In this work, we studied the doping of the WB_{4.2} boride with transition metals, and elucidated the electronic effects associated with this doping, in relation to material's hardness. We

identified substitutional doping in place of W atoms as strongly preferred over occupying the voids in the structure, for all impurities.

Two major substitutional intrinsic hardening mechanisms were found in doped WB_{4,2}. The first mechanism is associated with small radius elements (4th period elements, such as Ti, V, Cr, and Mn), with low energy 3d and 4s valence orbitals and smaller size. These elements bind poorly to the boron, both in the B₃ clusters and in the B_{hex} layers, but due to their small size allow the boron hexagonal layers to come closer. Smaller inter-layer distance allows for the stronger B_{hex} — $B_{cluster}$ bonding, increasing hardness. This small-size effect is the strongest when the impurity is closest to the B₃ cluster. The second mechanism is associated with large radius elements (5th and 6th period elements), with high-energy nd and (n + 1)s valence orbitals. Large radius elements bind strongly to the hexagonal boron layers and also form weaker bonds to the B₃ clusters. Despite slight weakening of the B_{hex} — $B_{cluster}$ bonds due to increased inter-layer separation in the material, large impurities form strong B_{hex} —M bonds, likely responsible for the enhanced intrinsic hardness. Large-size effect is the strongest when the impurity is farthest from the B₃ cluster, such that the $B_{cluster}$ —M bonding is minimal, B_{hex} — $B_{cluster}$ bonding is intact, and the B_{hex} —M bonding is maximal.

Importantly, despite $B_{\text{hex}}-B_{\text{cluster}}$ being the strongest inter-layer bond in the material, stronger than any $B_{\text{hex}}-M$ or $B_{\text{hex}}-W$ bonds, the increase in $B_{\text{hex}}-M$ bond strength for large impurities is roughly an order or magnitude greater than the increase in $B_{\text{hex}}-B_{\text{cluster}}$ bond strength for small impurities. Hence, $B_{\text{hex}}-M$ bonding is not to be ignored. Further studies are needed to assess these effects in the context of larger and more realistic unit cells, and varying placements and concentrations of the boron clusters and the impurities.

Acknowledgement

This work was supported by the NSF CAREER Award CHE-1351968 to A.N.A.. Computational resources were provided by XSEDE supported by the National Science Foundation

grant ACI-1548562, and the Hoffman Shared Cluster provided by UCLA Institute for Digital Research and Education's Research Technology Group. The work was performed in part as a final project in the Chem 126/226 class, "Computational Methods for Chemists". K.D.S., Z.M., H.Y., P.P., S.N., I.L., C.J., and I.W. were students in this class, and thank Dr. Max Kopelevich for technical support. A.N.A. thanks Prof. Alexander I. Boldyrev for mentorship and friendship over the years, and for inspiring her work on the chemical bonding in boron-containing systems, as well as her approach to education and mentoring.

Supporting Information Available

Includes detailed reasoning for the choice of DFT functional as well as additional geometric, thermodynamic, and QTAIM properties for doped model structures.

References

- (1) Tian, Y.; Xu, B.; Zhao, Z. Microscopic theory of hardness and design of novel superhard crystals. *Int. J. Refract. Met. Hard Mater.* **2012**, *33*, 93–106.
- (2) Akopov, G.; Yeung, M. T.; Kaner, R. B. Rediscovering the Crystal Chemistry of Borides. Adv. Mater. 2017, 29, 1604506.
- (3) Gu, Q.; Krauss, G.; Steurer, W. Transition Metal Borides: Superhard versus Ultra-incompressible. *Adv. Mater.* **2008**, *20*, 3620–3626.
- (4) Akopov, G.; Pangilinan, L. E.; Mohammadi, R.; Kaner, R. B. Perspective: Superhard metal borides: A look forward. *APL Mater.* **2018**, *6*.
- (5) Chung, H.-Y.; Weinberger, M. B.; Levine, J. B.; Kavner, A.; Yang, J.-M.; Tolbert, S. H.; Kaner, R. B. Synthesis of Ultra-Incompressible Superhard Rhenium Diboride at Ambient Pressure. *Science* 2007, 316, 436–439.

- (6) Chung, H.-Y.; Weinberger, M. B.; Levine, J. B.; Cumberland, R. W.; Kavner, A.; Yang, J.-M.; Tolbert, S. H.; Kaner, R. B. Response to Comment on "Synthesis of Ultra-Incompressible Superhard Rhenium Diboride at Ambient Pressure". Science 2007, 318, 1550d–1550d.
- (7) Mohammadi, R.; Lech, A. T.; Xie, M.; Weaver, B. E.; Yeung, M. T.; Tolbert, S. H.; Kaner, R. B. Tungsten tetraboride, an inexpensive superhard material. *Proc. Natl. Acad. Sci.* 2011, 108, 10958–10962.
- (8) Yeung, M. T.; Lei, J.; Mohammadi, R.; Turner, C. L.; Wang, Y.; Tolbert, S. H.; Kaner, R. B. Superhard Monoborides: Hardness Enhancement through Alloying in W_{1-x}Ta_xB. Adv. Mater. 2016, 28, 6993–6998.
- (9) Lei, J.; Yeung, M. T.; Mohammadi, R.; Turner, C. L.; Yan, J.; Kaner, R. B.; Tolbert, S. H. Understanding the mechanism of hardness enhancement in tantalum-substituted tungsten monoboride solid solutions. J. Appl. Phys. 2019, 125, 082529.
- (10) Long, Y.; Wu, Z.; Zheng, X.; Lin, H. T.; Zhang, F. Mechanochemical synthesis and annealing of tungsten di- and tetra-boride. *J. Am. Ceram. Soc.* **2019**, 1–8.
- (11) Xie, M.; Mohammadi, R.; Turner, C. L.; Kaner, R. B.; Kavner, A.; Tolbert, S. H. Exploring hardness enhancement in superhard tungsten tetraboride-based solid solutions using radial X-ray diffraction. Appl. Phys. Lett. 2015, 107, 041903.
- (12) Miao, N.; Sa, B.; Zhou, J.; Sun, Z. Theoretical investigation on the transition-metal borides with Ta₃B₄-type structure: A class of hard and refractory materials. *Comput. Mater. Sci.* **2011**, *50*, 1559–1566.
- (13) Mohammadi, R.; Xie, M.; Lech, A. T.; Turner, C. L.; Kavner, A.; Tolbert, S. H.; Kaner, R. B. Toward Inexpensive Superhard Materials: Tungsten Tetraboride-Based Solid Solutions. J. Am. Chem. Soc. 2012, 134, 20660–20668.

- (14) Akopov, G.; Yeung, M. T.; Roh, I.; Sobell, Z. C.; Yin, H.; Mak, W. H.; Khan, S. I.; Kaner, R. B. Effects of Dodecaboride-Forming Metals on the Properties of Superhard Tungsten Tetraboride. *Chem. Mater.* 2018, 30, 3559–3570.
- (15) Akopov, G.; Roh, I.; Sobell, Z. C.; Yeung, M. T.; Kaner, R. B. Investigation of ternary metal dodecaborides $(M_1M_2M_3)B_{12}$ $(M_1, M_2 \text{ and } M_3 = Zr, Y, Hf \text{ and Gd})$. Dalt. Trans. **2018**, 47, 6683–6691.
- (16) Akopov, G.; Sobell, Z. C.; Yeung, M. T.; Kaner, R. B. Stabilization of LnB_{12} (Ln = Gd, Sm, Nd, and Pr) in $Zr_{1-x}Ln_xB_{12}$ under Ambient Pressure. *Inorg. Chem.* **2016**, *55*, 12419–12426.
- (17) Mohammadi, R.; Turner, C. L.; Xie, M.; Yeung, M. T.; Lech, A. T.; Tolbert, S. H.; Kaner, R. B. Enhancing the Hardness of Superhard Transition-Metal Borides: Molybdenum-Doped Tungsten Tetraboride. Chem. Mater. 2016, 28, 632–637.
- (18) Akopov, G.; Yeung, M. T.; Turner, C. L.; Mohammadi, R.; Kaner, R. B. Extrinsic Hardening of Superhard Tungsten Tetraboride Alloys with Group 4 Transition Metals. J. Am. Chem. Soc. 2016, 138, 5714–5721.
- (19) Lech, A. T.; Turner, C. L.; Mohammadi, R.; Tolbert, S. H.; Kaner, R. B. Structure of superhard tungsten tetraboride: A missing link between MB₂ and MB₁₂ higher borides. *Proc. Natl. Acad. Sci.* 2015, 112, 3223–3228.
- (20) Kvashnin, A. G.; Rybkovskiy, D. V.; Filonenko, V. P.; Bugakov, V. I.; Zibrov, I. P.; Brazhkin, V. V.; Oganov, A. R.; Osiptsov, A. A.; Zakirov, A. Y. WB_{5-x}: Synthesis, Properties, and Crystal Structure—New Insights into the Long-Debated Compound. Adv. Sci. 2020, 7, 2000775.
- (21) Dong, J.; Li, H.; Wang, J.; Guo, Z.; Liao, J.; Hao, X.; Zhang, X.; Chen, D. Nonrandomly Distributed Tungsten Vacancies and Interstitial Boron Trimers in Tungsten Tetraboride.

 J. Phys. Chem. C 2019, 123, 29314–29323.

- (22) Gong, W.; Liu, C.; Song, X.; Li, Q.; Ma, Y.; Chen, C. Unravelling the structure and strength of the highest boride of tungstent WB_{4,2}. *Phys. Rev. B* **2019**, *100*, 220102.
- (23) Perdew, J. P.; Burke, K.; Ernzerhof, M. Generalized Gradient Approximation Made Simple. *Phys. Rev. Lett.* **1996**, *77*, 3865–3868.
- (24) Perdew, J. P.; Burke, K.; Ernzerhof, M. Errata: Generalized Gradient Approximation Made Simple. *Phys. Rev. Lett.* **1997**, *78*, 1396–1396.
- (25) Grimme, S.; Antony, J.; Ehrlich, S.; Krieg, H. A consistent and accurate ab initio parametrization of density functional dispersion correction (DFT-D) for the 94 elements H-Pu. J. Chem. Phys. 2010, 132, 154104.
- (26) Kresse, G.; Hafner, J. Ab initio molecular dynamics for liquid metals. *Phys. Rev. B* **1993**, 47, 558–561.
- (27) Kresse, G.; Hafner, J. Ab initio molecular-dynamics simulation of the liquid-metal—amorphous-semiconductor transition in germanium. *Phys. Rev. B* **1994**, *49*, 14251–14269.
- (28) Kresse, G.; Furthmüller, J. Efficient iterative schemes for ab initio total-energy calculations using a plane-wave basis set. *Phys. Rev. B* **1996**, *54*, 11169–11186.
- (29) Kresse, G.; Furthmüller, J. Efficiency of ab-initio total energy calculations for metals and semiconductors using a plane-wave basis set. *Comput. Mater. Sci.* **1996**, *6*, 15–50.
- (30) Tian, Y.; Xu, B.; Zhao, Z. Microscopic theory of hardness and design of novel superhard crystals. *Int. J. Refract. Met. Hard Mater.* **2012**, *33*, 93–106.
- (31) Otero-de-la Roza, A.; Blanco, M.; Pendás, A. M.; Luaña, V. Critic: a new program for the topological analysis of solid-state electron densities. *Comput. Phys. Commun.* 2009, 180, 157–166.

- (32) Otero-de-la Roza, A.; Johnson, E. R.; Luaña, V. Critic2: A program for real-space analysis of quantum chemical interactions in solids. *Comput. Phys. Commun.* **2014**, 185, 1007–1018.
- (33) Yu, M.; Trinkle, D. R. Accurate and efficient algorithm for Bader charge integration. *J. Chem. Phys.* **2011**, *134*, 064111.
- (34) Deringer, V. L.; Tchougréeff, A. L.; Dronskowski, R. Crystal Orbital Hamilton Population (COHP) Analysis As Projected from Plane-Wave Basis Sets. J. Phys. Chem. A 2011, 115, 5461–5466.
- (35) Maintz, S.; Deringer, V. L.; Tchougréeff, A. L.; Dronskowski, R. Analytic projection from plane-wave and PAW wavefunctions and application to chemical-bonding analysis in solids. *J. Comput. Chem.* **2013**, *34*, 2557–2567.
- (36) Maintz, S.; Deringer, V. L.; Tchougréeff, A. L.; Dronskowski, R. LOBSTER: A tool to extract chemical bonding from plane-wave based DFT. *J. Comput. Chem.* **2016**, *37*, 1030–1035.
- (37) Nelson, R.; Ertural, C.; George, J.; Deringer, V. L.; Hautier, G.; Dronskowski, R. LOBSTER: Local orbital projections, atomic charges, and chemical-bonding analysis from projector-augmented-wave-based density-functional theory. J. Comput. Chem. 2020, 41, 1931–1940.
- (38) Clementi, E.; Raimondi, D. L.; Reinhardt, W. P. Atomic Screening Constants from SCF Functions. II. Atoms with 37 to 86 Electrons. J. Chem. Phys. 1967, 47, 1300–1307.
- (39) Kotochigova, S.; Levine, Z. H.; Shirley, E. L.; Stiles, M. D.; Clark, C. W. Local-density-functional calculations of the energy of atoms. *Phys. Rev. A* **1997**, *55*, 191–199.
- (40) Kotochigova, S.; Levine, Z. H.; Shirley, E. L.; Stiles, M. D.; Clark, C. W. Erratum:

- Local-density-functional calculations of the energy of atoms [Phys. Rev. A 55, 191 (1997)]. Phys. Rev. A 1997, 56, 5191–5192.
- (41) Kotochigova, S. K.; Levine, Z. H.; Shirley, E. L.; Stiles, M. D.; Clark, C. W. C. Atomic Reference Data for Electronic Structure Calculations. 2009.
- (42) Martin W. S., W. W. L. In *At. Mol. Opt. Phys. Handb.*; Drake, G. G. W., Ed.; AIP Press: Woodbury, NY, 1996; Chapter 10, pp 135–153.

TOC Graphic

